DOI 10.1007/s11182-023-02772-z
Russian Physics Journal, Vol. 65, No. 8, December, 2022 (Russian Original No. 8, August, 2022)

STRUCTURE EFFECT ON THE DIFFUSION AND ACCUMULATION OF HYDROGEN IN THE Zr–1Nb ALLOY

G. P. Grabovetskaya,[1] E. N. Stepanova,[2] N. N. Nikitenkov,[2] I. P. Mishin,[1] V. A. Vinokurov,[1] V. S. Sypchenko,[2] and V. N. Kudiiarov[2]

UDC 539.219.3:546.11:546.831

Comparative studies of the diffusion and accumulation of hydrogen in the Zr*–1 wt.%* Nb *alloy in the fine-grained and ultrafine-grained states during electrolytic saturation were carried out by the membrane method. The formation of an ultrafine-grained structure is established to lead to a decrease in the effective diffusion coefficient and the rate of hydrogen accumulation in the bulk of the alloy. The influence of the dislocation density and the length of grain boundaries on the effective diffusion coefficient of hydrogen and the ability of the alloy to accumulate hydrogen in the bulk are considered.*

Keywords: zirconium alloy, ultrafine-grained structure, diffusion, hydrogen, membrane method.

INTRODUCTION

The presence of interstitial impurities in metals has a significant effect on their operational characteristics. In hydride-forming metals, hydrogen occupies a special place among interstitial impurities in terms of its effect on physical and mechanical properties [1–4]. This is due to the fact that due to the high diffusion mobility in metals, hydrogen can be redistributed in the volume of the material under the action of elastic stress fields, forming accumulations in the most stressed areas and thereby increasing the probability of plastic deformation localization, hydride precipitation, and the formation of pores and cracks [5–7]. It is known [8–10] that the diffusion of hydrogen in a metal depends not only on the type of the crystal lattice of the metal, but also on the degree of its perfection. The diffusion of hydrogen in metallic materials is affected by such defects as vacancies, impurity atoms, dislocations, as well as grain and phase boundaries.

Recently, ultrafine-grained (UFG) metallic materials have been actively developed and studied. This is due to the fact that by forming the UFG structure, it is possible to significantly improve the physicomechanical and operational characteristics of metallic materials at low homologous temperatures [11–13]. In addition, metallic materials in the UFG state are considered as promising materials for hydrogen storage and transportation [14]. Metallic materials with UFG structure have a large length of grain boundaries and often a high density of such crystal lattice defects as dislocations and vacancies. According to the data given in [12, 15, 16], the volume fraction of boundaries in UFG metallic materials obtained by severe plastic deformation (SPD) is 0.1–1%, and the dislocation density is 10^{14}–10^{15} m^{-2}. The relative concentration of vacancies in such materials can reach 10^{-4} [15, 16]. (In well-annealed metals, the dislocation density is 10^{8}–10^{10} m^{-2}, and the relative concentration of vacancies is 10^{-23}–10^{-22} [15, 16].) Grain boundaries and crystal lattice defects can be traps for hydrogen [8, 9], which reduces the rate of hydrogen diffusion in the metal. On the other hand,

[1]Institute of Strength Physics and Materials Science of the Siberian Branch of the Russian Academy of Sciences, Tomsk, Russia, e-mail: grabg@ispms.ru; mip@ispms.tsc.ru; vinokurov_old@yandex ru; [2]National Research Tomsk Polytechnic University, Tomsk, Russia, e-mail: enstepanova@tpu.ru; nikitenkov@tpu ru; sypchenko@tpu.ru; kudiyarov@tpu.ru. Translated from Izvestiya Vysshikh Uchebnykh Zavedenii, Fizika, No. 8, pp. 98–105, August, 2022. Original article submitted April 11, 2022; revision submitted June 30, 2022.

there are data [17–19] according to which the rate of hydrogen diffusion along grain boundaries and dislocations is higher than the rate of diffusion along the crystal lattice. Therefore, it is of interest to compare the development of hydrogen diffusion in a material with fine-grained (FG) and UFG structures.

The purpose of this work is to study the influence of the formation of UFG structure on the effective diffusion coefficients and the ability to accumulate hydrogen in the bulk of the zirconium Zr–1 wt. % Nb alloy (hereinafter, the Zr–1Nb alloy).

MATERIAL AND RESEARCH METHODS

The starting material for the study was a Zr–1Nb alloy with the following elemental composition (wt.%): 1Nb+Fr < 0.05+O < 0.09+0.001H and the rest is Zr. As delivered, the alloy has a polycrystalline structure with an average grain size of ~5 μm. In addition to the main phase α-Zr (hcp), the alloy contains secondary phases β-Nb (bcc) and β-Zr (bcc), the volume fraction of which does not exceed ~2.5 vol.% [4]. Secondary phases in the form of particles ranging in size from several tens of nanometers to microns are observed in the bulk and at grain boundaries.

The UFG structure in the alloy was obtained by one of the SPD methods according to the scheme of uniaxial compression with a change in the deformation axis (*abc*-pressing). Pressing was carried out at room temperature with intermediate annealings at 803 K for 30 min. The pressing rate was ~10^{-3} s^{-1}. The alloy was pressed in four cycles. One cycle consisted of three pressings. The deformation for one pressing was 40–50%.

The structure of the alloy was studied using the Olympus GX-71 optical and JEM-2100 transmission electron microscopes. The sizes of structural elements were measured in photographs of the microstructure by the secant method [20]. The samples for the FG and UFG states were at least 70 and 170 elements, respectively.

The phase composition, the value of crystal lattice microdistortions (Δε), and the sizes of coherent scattering regions (*D*) in the alloy were determined by standard methods of X-ray diffraction analysis using a Shimadzu XRD-7000 diffractometer in CuK_α radiation. The diffraction patterns were interpreted using the PowderCell program. The density of dislocations was determined from the broadening of the diffraction maxima at half height based on the Cauchy approximation. To separate the contributions of *D* and Δε to the broadening of diffraction peaks, we used the diffraction peaks of the $(101)_\alpha$ and $(103)_\alpha$ planes. The calculation of the total dislocation density (ρ), caused by the value of Δε ($\rho_1 = k\Delta\varepsilon^2/b^2$) and the presence of coherent scattering regions ($\rho_2 = 3/D^2$ $\rho_2 = 3/D^2$), was carried out according to the formula [21]

$$\rho = \left(\frac{3}{D^2} \frac{k\Delta\varepsilon^2}{b^2} \right)^{1/2}, \quad (1)$$

where *b* is the Burgers vector ($3.23 \cdot 10^{-10}$ m [22]), *k* is a constant associated with the elastic properties of the material (for zirconium, *k* ~16 [23]).

The influence of the Zr–1Nb alloy structure on the hydrogen diffusion was studied by the membrane method [24, 25]. The experimental setup made it possible to combine an electrolytic cell through a membrane (to saturate the sample with hydrogen) and a high-vacuum chamber containing a mass spectrometer (MX-7304) [26].

The Zr–1Nb alloy foils in the FG and UFG states were used as membranes. The foils were 20 mm in diameter and 58–61 μm thick. Plates for foils were cut from blanks by the electrospark method. The plates were thinned by mechanical grinding, multi-pass reverse rolling by 40–50%, and chemical polishing. Previously, it was found that the dimensions of the UFG structure elements in the Zr–1Nb alloy are stable up to a temperature of 773 K [4]. Therefore, to change the density of defects, the membranes with the FG structure and part of the membranes with the UFG structure were annealed at a temperature of 673 K in a vacuum of $5 \cdot 10^{-3}$ Pa for 1 h.

Electrolyte 0.1 M H_2SO_4 was used for electrolysis. The electrolysis current density was 1 $A \cdot cm^{-2}$, the initial pressure in the vacuum chamber was 10^{-5} Pa. During electrolysis, the membrane was slowly heated up to a temperature of ~333 K for one hour. Further, the temperature remained constant. After switching on the electrolytic cell, when signs of an increase in the intensity of hydrogen lines appeared, the time, elapsed from the moment the electrolysis was

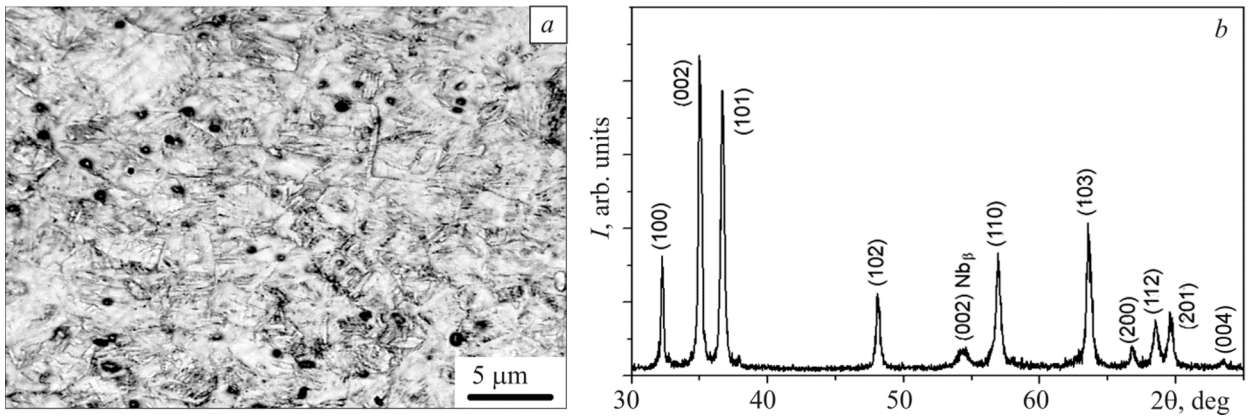

Fig. 1. Microstructure (*a*) and part of the diffraction pattern (*b*) of the fine-grained Zr–1Nb alloy.

switched on (t_e), was recorded. The change in the intensity of the mass lines of the following elements and compounds in the vacuum chamber was monitored: H, H_2, CH, and OH. In what follows, only the H_2 line will be discussed. The effective diffusion coefficient of hydrogen (D_H) was estimated using the formula [24]

$$D_H = l^2 / 6t_e, \quad (2)$$

where l is the membrane thickness.

The hydrogen concentration in the membranes was measured after the hydrogen intensity lines reached saturation using an RHEN 602 hydrogen gas analyzer with an accuracy of 0.0001 wt.%. To do this, the membranes were removed from the electrolyte–vacuum gap.

The effect of the UFG structure on the rate of saturation of the Zr–1Nb alloy with hydrogen at an elevated temperature was studied by heating the samples in a dry hydrogen medium. The sample heating rate was 12°C/min, the hydrogenation time was 1 h. Plates with an area of 10 × 15 mm^2 and a thickness of 1 mm were used as samples. The surface of the samples was subjected to grinding and chemical polishing. Samples were saturated with hydrogen at temperatures of 673 and 773 K and a pressure of 0.66 atm in a PCIM Sievert-type setup with automatic recording of the saturation curve [27]. In the present experiment, the error in determining the hydrogen concentration in the samples during hydrogenation was 0.01 wt.%. The error was determined based on the accuracy of determining the main thermodynamic parameters (temperature and pressure), calibration accuracy, and a series of measurements.

RESULTS AND DISCUSSION

Figure 1 shows the microstructure and a part of the diffraction pattern of the Zr–1Nb alloy foil in the FG state. As a result of the foil preparation, the morphology of the alloy structure does not change compared to the initial state. At the boundaries and in the volume of the alloy grains, particles of precipitates of other phases are visible. Only two phases, α-Zr and β-Nb, are detected in the foil by X-ray diffraction analysis (Fig. 1*b*). A texture of the (002) α-Zr type is observed in the foil.

A typical electron microscopic image of the structure of a Zr–1Nb alloy foil in the UFG state is shown in Fig. 2. In the bright-field image of the UFG structure, grain boundaries are not revealed. At the same time, the dark-field image shows that the UFG structure of the foil consists of separate elements (Fig. 2*b*).

The microdiffraction pattern of the UFG structure at a selector diaphragm diameter of ~1.4 μm is annular-ring (Fig. 2*c*), which is typical of UFG materials obtained by SPD. The rings in the microdiffraction pattern belong to the α-phase of zirconium. This indicates the presence in the structure of a large number of elements of this phase per unit volume and a significant misorientation between them. The average size of the elements of the UFG structure,

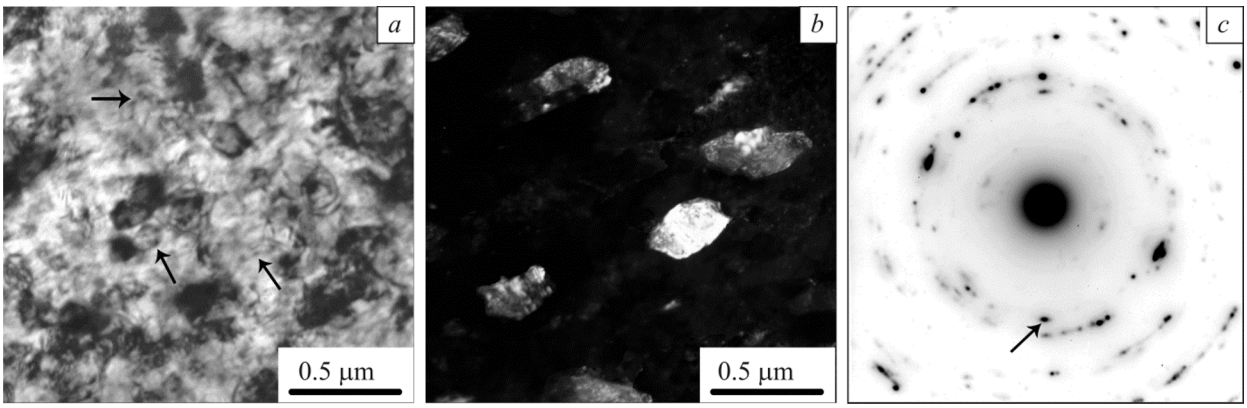

Fig. 2. Electron microscopic images of the microstructure of the UFG Zr–1Nb alloy in the state after SPD: bright-field (*a*), dark-field recorded in the $(100)_\alpha$ reflection (*b*) (in the microdiffraction pattern, the reflection is indicated by an arrow), and microdiffraction pattern (*c*). (Arrows in the bright field indicate segregations of secondary phases).

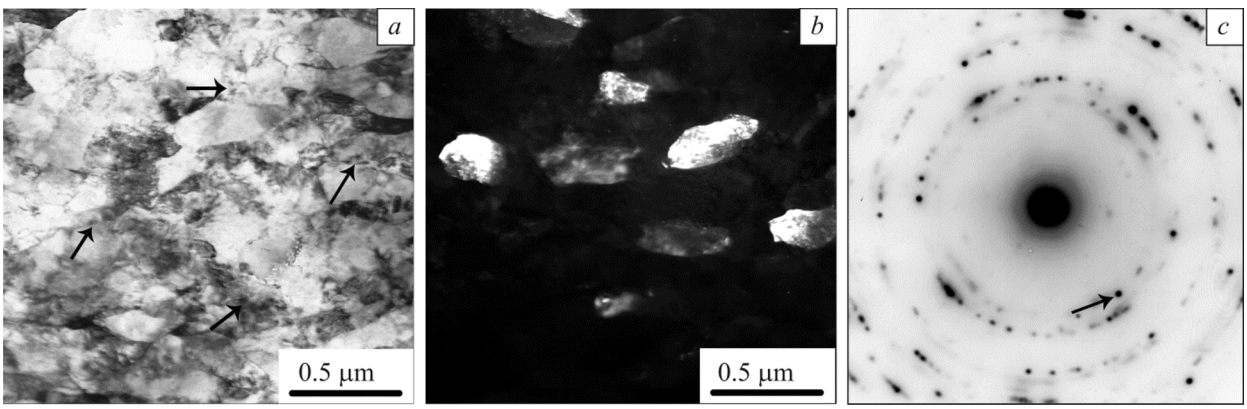

Fig. 3. Electron microscopic image of the microstructure of the UFG Zr–1Nb alloy in the state after annealing at a temperature of 673 K for 1 h: bright field (*a*), dark field recorded in the $(100)_\alpha$ reflection (*b*) (in the microdiffraction pattern, the reflection is indicated by an arrow), and microdiffraction pattern (*c*). (Arrows in the bright field indicate segregations of secondary phases).

determined from the dark-field image, is (0.3±0.12) μm. Nanosized particles of secondary phases are observed in the volume of the foil. According to [20], the formation of the UFG structure with the indicated size of elements increases the length of boundaries per unit area in the Zr–1Nb alloy by an order of magnitude compared to the FG structure.

Figure 3 shows an electron microscopic image of the structure of the Zr–1Nb alloy foil in the UFG state after annealing at a temperature of 673 K for 1 h. As noted above, such annealing does not change the average size of elements of the grain–subgrain structure of the UFG Zr–1Nb alloy (Figs. 3*a* and 3*b*). At the same time, after this annealing, grains with clear boundaries appear in the structure (Fig. 3*a*), which indicates a decrease in internal stresses. The microdiffraction pattern (Fig. 3*c*) of the UFG structure at a selector diaphragm diameter of 1.4 μm also shows rings belonging to the α-zirconium phase. Particles of secondary phases are present at the boundaries and in the volume of grains.

Portions of the diffraction patterns of foils of the UFG Zr–1Nb alloy before and after annealing at a temperature of 673 K for 1 h are shown in Fig. 4. In both cases, only the α-Zr phase is detected in the UFG structure of the Zr–1Nb alloy by X-ray diffraction analysis. In foils with the UFG structure, as in a foil with the FG structure, a texture of the

TABLE 1. Size of Structural Elements (d), Magnitude of Crystal Lattice Microdistortions ($\Delta\varepsilon$) of the Coherent Scattering Region (D), and Dislocation Density (ρ) in Zr–1Nb Alloy Foils

Material	d, μm	$\Delta\varepsilon$, 10^{-3}	D, nm	ρ, m^{-2}
FG Zr–1Nb	5	0.12	122	$1.7\cdot10^{13}$
UFG Zr–1Nb	0.3	2.4	36	$1.4\cdot10^{15}$
UFG Zr–1Nb, annealing 673 K for 1 h	0.3	0.18	98	$3.9\cdot10^{13}$

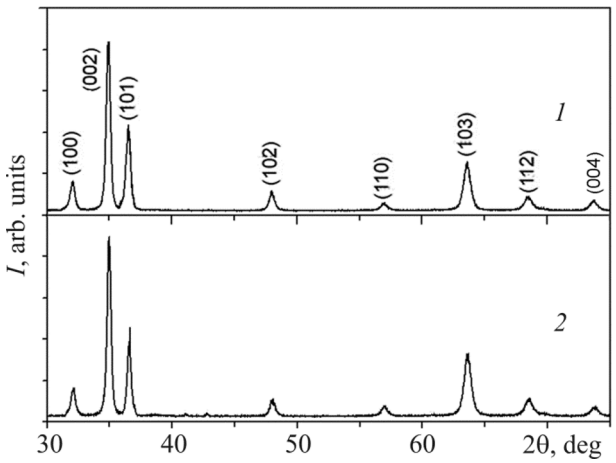

Fig. 4. Portions of X-ray diffraction patterns of the UFG Zr–1Nb alloy in the state after SPD (*1*) and after annealing at 673 K for 1 h (*2*).

(002) α-Zr type is observed. The absence of diffraction maxima of the secondary phases in the diffraction patterns is apparently due to the higher texturization of the α-Zr phase in the UFG structure compared to the FG structure. Comparison of the diffraction patterns of the UFG structure before and after annealing at a temperature of 673 K for 1 h shows that the texture of the alloy after annealing does not change.

This confirms the absence of a noticeable process of recrystallization and grain growth in the UFG structure during the indicated annealing. At the same time, annealing at a temperature of 673 K for 1 h leads to a decrease in the broadening of the diffraction peaks, which indicates a decrease in the defect density and the magnitude of internal stresses in the UFG structure.

The values of ρ and $\Delta\varepsilon$ in the studied foils of the Zr–1Nb alloy calculated from the diffraction patterns (Figs. 1 and 4) are presented in Table 1. It can be seen from Table 1 that the value of ρ in the UFG structure in the state immediately after SPD is almost two orders of magnitude higher, and the value of $\Delta\varepsilon$ is an order of magnitude higher than the corresponding values for the FG structure. As a result of annealing at 673 K for 1 h, the values of ρ and $\Delta\varepsilon$ in the UFG structure decrease to values close to the corresponding values in the FG structure.

Figure 5 shows the normalized curves which demonstrate the change in the content of hydrogen (H_2) in the vacuum chamber passed through the membranes of the FG and UFG Zr–1Nb alloys during electrolysis (the initial level of hydrogen in the vacuum chamber was taken as a unit). It can be seen that the incubation period of the hydrogen penetration through the alloy membranes in the UFG state is 1.8–2.3 times longer than that in the FG state.

Table 2 shows the rate at which the hydrogen content reaches a stationary level (V_H) in the vacuum chamber and the effective hydrogen diffusion coefficients (D_H) in the Zr–1Nb alloy in various structural states calculated by formula (2). Here, the D_H value for the Zr–1Nb FG alloy, determined in [28] by studying the distribution of hydrogen over the depth of the sample after its partial saturation with hydrogen or partial degassing, is also given. It can be seen that the D_H value obtained in this work for the FG Zr–1Nb alloy is in good agreement with the data of [28]. Table 2

TABLE 2. Effective Diffusion Coefficient of Hydrogen (D_H) and the Rate at which the Hydrogen Content in the Vacuum Chamber Reaches a Stationary Level (V_H) in Zr–1Nb Alloy Membranes in the FG and UFG States (Temperature 333 K)

Material	Membrane thickness, μm	$V_H \cdot 10^3$, rel. units/min	D_H, m^2/s
FG Zr–1Nb			$4.1 \cdot 10^{-14}$ [28]
FG Zr–1Nb	60	4.7	$3.3 \cdot 10^{-14}$
UFG Zr–1Nb	61	1.5	$1.4 \cdot 10^{-14}$
UFG Zr–1Nb, annealing 673 K for 1 h	58	2.1	$1.7 \cdot 10^{-14}$

TABLE 3. Saturation Rate and Hydrogen Concentration in Zr–1Nb Alloy Membranes in the FG and UFG States when the Hydrogen Content in the Chamber Reaches a Stationary Level (Temperature 333 K)

Material	Saturation rate $\cdot 10^5$, wt.%/min	Hydrogen concentration, wt.%	
		Initial state	State after electrolysis
FG Zr–1Nb	1.86	0.0014	0.0081
UFG Zr–1Nb	1.62	0.0017	0.0156
UFG Zr–1Nb annealing 673 K for 1 h	1.7	0.0013	0.0129

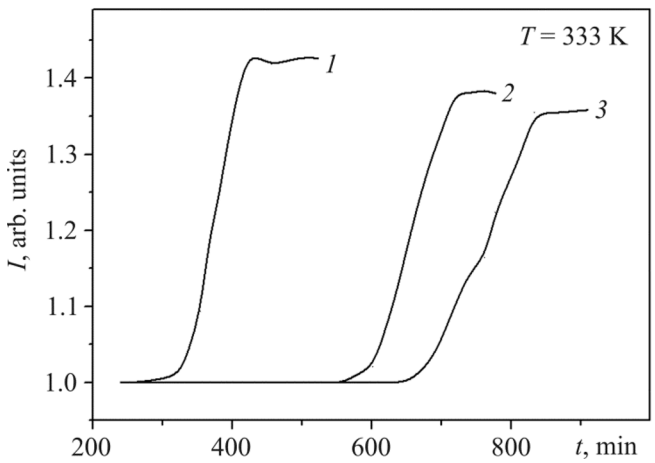

Fig. 5. Curves of changes in the hydrogen concentration in the vacuum chamber depending on the time of electrolysis of the Zr–1Nb alloy in FG (*1*) and UFG (*2*, *3*) states. (Curve *3* corresponds to UFG Zr–1Nb alloy after annealing at 673 K, 1 h).

shows that as a result of the formation of the UFG structure, the D_H value of the Zr–1Nb alloy decreases by about 2.5 times, and the V_H value decreases by about 3 times. Annealing of the UFG alloy at a temperature of 673 K for 1 h, which reduces ρ and Δε, leads to an increase in D_H and V_H. However, even after annealing, the values of D_H and V_H remain significantly lower than the corresponding values for the FG state.

Table 3 shows the saturation rate and hydrogen concentration in the membranes when the hydrogen content in the chamber reaches a stationary level (full saturation level). It can be seen that the hydrogen concentration in the membranes with the UFG structure is 1.6–2 times higher than the concentration in the membrane with the FG structure.

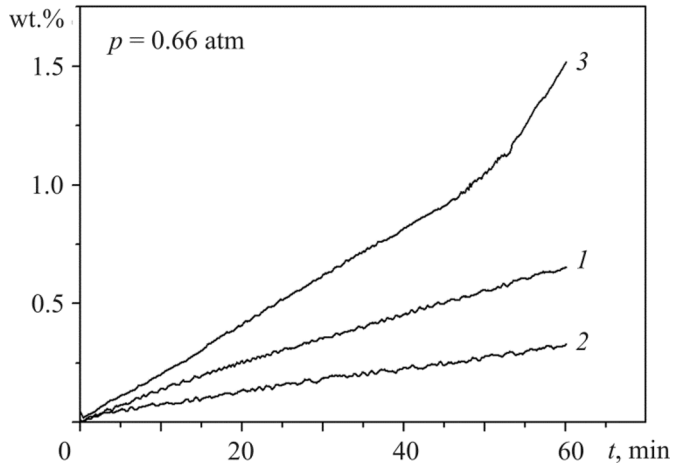

Fig. 6. Kinetic curves of hydrogen saturation of the Zr–1Nb alloy in FG (*1*) and UFG (*2*, *3*) states during heating in a hydrogen atmosphere at temperatures of 673 K (*1*, *2*) and 773 K (*3*).

At the same time, the hydrogen saturation rate of membranes with the UFG structure is lower compared to the corresponding value for the membrane with the FG structure.

The observed decrease in the values of D_H and V_H in the Zr–1Nb alloy in the UFG state as compared to the FG state is consistent with the existing concept that crystal lattice defects are traps for hydrogen and prevent its diffusion into the bulk of the material [8–10]. Traps for hydrogen in the Zr–1Nb alloy in both states are vacancies, dislocations, and grain boundaries. In the UFG Zr–1Nb alloy in the state after SPD, the density of these traps is significantly higher than that in the FG state (Table 1). Annealing at a temperature of 673 K for 1 h does not change the grain size in the UFG Zr–1Nb alloy and, consequently, the density of grain boundaries in its bulk. However, the annealing leads to a decrease in ρ to a value of $3.9 \cdot 10^{13}$ m^{-2}, close to the value for the FG state ($1.7 \cdot 10^{13}$ m^{-2}). The relative concentration of vacancies during annealing at a temperature of 673 K for 1 h can also decrease to values close to those for the FG state. It is known that the stage of annealing of vacancies in UFG materials obtained by SPD methods is observed at the same or lower temperature as compared to the stage of annealing of dislocations [15, 16]. At the same time, the D_H and V_H values of the Zr–1Nb alloy in the UFG state after annealing remain significantly lower than the corresponding values for the FG state (Table 2). In addition, it can be seen from Table 3 that the hydrogen concentration in the membrane with the UFG structure in the state after annealing, when the hydrogen content in the vacuum chamber reaches saturation, is 1.9 times higher than that in the membrane with the FG structure. Thus, the results obtained suggest that the main traps for hydrogen in the UFG structure are grain boundaries.

This assumption is consistent with the results of a comparative study of the saturation of the Zr–1Nb alloy with hydrogen during heating in a dry hydrogen medium under conditions of stability (temperature 673 K [4]) and under conditions of average grain size growth in the UFG structure (temperature 773 K [4]). Figure 6 shows the kinetic curves of hydrogen saturation of the Zr–1Nb alloy in the FG and UFG states during heating in a dry hydrogen medium at temperatures of 673 and 773 K for 1 h. It can be seen that upon heating under conditions of stability of the average grain size, the kinetic curve of hydrogen saturation of the Zr–1Nb alloy in the UFG state (curve *2*) is monotonic, as is the case for the alloy in the FG state (curve *1*). The Zr–1Nb alloy in the UFG state has a lower hydrogen accumulation rate compared to the FG state. After this heating, the hydrogen concentration in the Zr–1Nb alloy in the UFG and FG states is 0.32 and 0.63 wt.%, respectively. Upon heating in a hydrogen medium at a temperature of 773 K for 1 h, the saturation kinetic curve of the UFG Zr–1Nb alloy becomes nonmonotonic: with an increase in the grain size, the rate of the hydrogen saturation of the alloy increases (curve *3*).

CONCLUSIONS

The formation of an ultrafine-grained structure leads to a decrease in the effective diffusion coefficient of hydrogen in the Zr–1Nb alloy. The rate of hydrogen accumulation in the bulk of the Zr–1Nb alloy with an ultrafine-grained structure is lower, and the ability to accumulate hydrogen in the bulk upon reaching saturation is higher compared to the corresponding values for an alloy with a fine-grained structure. The main traps for hydrogen in the ultrafine-grained Zr–1Nb alloy are the grain boundaries. A decrease in the effective diffusion coefficient of hydrogen and an increase in the ability to accumulate hydrogen in the bulk of the alloy with an ultrafine-grained structure are mainly due to the greater length of grain boundaries.

The work was carried out within the framework of the state task of the ISPMS SB RAS, topic number FWRW-2021-0004, using the scientific equipment of the Tomsk Materials Science Center for Collective Use.

REFERENCES

1. H.-M. Tung, T.-C. Chen, and C.-C. Tseng, Mater. Sci. Eng. A, **659**, 172–178 (2016).
2. Y. Zhang, H. Qi, and X. Song, J. Nucl. Mater., **554**, 153082 (2021).
3. H. Lee, K.-M. Kim, J.-S. Kim, and Y.-S. Kim, Nucl. Eng. Technol., **52 (2)**, 352–359 (2020).
4. E. N. Stepanova, G. P. Grabovetskaya, and A. S. Dubrovskaya, Int. J. Hydrogen Energy, **42(35)**, 22633–22640 (2017).
5. B. A. Kolachev, Hydrogen Embrittlement of Metals [in Russian], Metallurgiya, Moscow (1985)
6. Yu. P. Sharkeev, E. V. Legostaeva, V. P. Vavilov, *et al*., Russ. Phys. J., **62**, No. 8, 1349–1356 (2019).
7. E. Stepanova, G. Grabovetskaya, M. Syrtanov, and I. Mishin, Metals, **10 (5)**, 592 (2020).
8. P. V. Geld, R. F. Ryabov, and E. S. Kodes, Hydrogen and Metal Structure Imperfections [in Russian], Metallurgiya, Moscow (1979).
9. A. Turnbull, Gaseous Hydrog. Embrittlement Mater. Energy Technol., Elsevier (2012).
10. N. A. Kulabukhova, G. M. Poletaev, M. D. Starostenkov, *et al*., Russ. Phys. J., **54**, No. 12, 1394–1400 (2012).
11. D. G. Morris, Mechanical Behavior of Nanostructured Materials, Trans. Tech. Publication ltd, Switherland (1998).
12. R. Z. Valiev, Y. Estrin, Z. Horita, *et al*., Mater. Res. Lett., **4**, 1–21 (2016).
13. E. N. Stepanova, G. P. Grabovetskaya, I. P. Mishin, and D.Yu. Bulynko, Mater. Today Proc., No. 2, 365–369 (2015).
14. A. Zuttel, Mater. Today, No. 9, 24–33 (2003).
15. M. J. Zehetbauer, G. Steiner, E. Schafler, *et al*., Mater. Sci. Forum, **503–504**, 57–64 (2006).
16. A. I. Lotkov, A. Baturin, V. N. Grishkov, and V. I. Kopylov, Phys. Mesomech., **10 (3−4)**,179–189 (2007).
17. M. Legros, G. Dehm, E. Arzt, and T. J. Balk, Science, **319 (5870)**, 1646–1649 (2008).
18. Hideaki Iwaoka, Makoto Arita, and Zenji Horita, Acta Mater., **107**, 168–177 (2016).
19. A. M. Brass and A. Chanfreau, Acta Mater., **44**, 3823–3831 (1996).
20. S. A. Saltykov, Stereometric Metallography [in Russian], Metallurgiya, Moscow (1970).
21. G. K. Williamson and R. E. Smallman, Phil. Mag., **1**, No. 1, 34–46 (1956).
22. P. M. Sargent and M. F. Ashby, Scripta Metall., **16**, No. 1, 1415–1422 (1982).
23. P. S. Chowdhury, P. Mukherjee, N. Gayathri, *et al*., Bull. Mater. Sci., **34**, No. 3, 507–513 (2011).
24. V. P, Baranov, Sovrem. Probl. Nauki I Obrazov., No. 1, 38–41 (2007).
25. I. S. Petriev, I. S. Lutsenko, P. D. Pushankina, *et al*., Russ. Phys. J., **65**, No. 2, 312–316 (2022).
26. N. N. Nikitenkov, A. M. Hashhash, Yu. I. Tyurin, *et al*., J. Surf. Investigat. X-ray, Synchrotron and Neutron Techniques, **4**, No. 3, 534–537 (2010).
27. V. N. Kudiiarov and A. M. Lider, Fundam. Issled., No. 10, 3466–3471 (2013).
28. S. V. Ivanova, Materialoved., No. 7, 42–49 (2002).